Catalytic flow with a coupled Finite Difference - Lattice Boltzmann scheme

Daniel Berger,[1,*] Ana-Sunčana Smith,[2,3] and Jens Harting[1,4]

[1] *Helmholtz Institute Erlangen-Nürnberg for Renewable Energy (IEK-11), Forschungszentrum Jülich, Fürther Straße 248, 90429 Nürnberg, Germany*

[2] *Institute for Theoretical Physics I, Friedrich-Alexander-University of Erlangen-Nürnberg, Nägelsbachstraße 49b, 91052 Erlangen, Germany*

[3] *Ruđer Bošković Institute, Bijenička cesta 54, P.P. 180, HR-10002 Zagreb, Croatia*

[4] *Department of Applied Physics, Eindhoven University of Technology, P. O. Box 513, 5600MB Eindhoven, The Netherlands*

(Dated: April 20, 2018)

Catalysis is one of the key technologies for a sustainable energy future with vast applications in chemical energy storage, efficient chemical conversion and reducing air pollution. Many catalyst devices employ porous or foam-like structures, which leads to a complex macroscopic mass and heat transport. To unravel the detailed dynamics of the reactive gas flow, we present a novel coupled finite differences thermal lattice Boltzmann model (FD-LBM): the thermal LBM is used to solve the heat and mass transport in the gas domain and the finite differences are augmented to solve the heat equation in the solid and across the gas-solid interface for a consistent treatment of the reaction enthalpy. The chemical surface reactions are incorporated in a flexible fashion through flux boundary conditions at the gas-solid interface. We scrutinize the thermal LBM by benchmarking the macroscopic transport in the gas domain as well as enthalpy conservation across the solid-gas interface. We exemplify the applicability of our model by simulating the reactive gas flow trough a microporous material catalysing the water-gas-shift reaction.

arXiv:submit/2235227 [physics.flu-dyn] 20 Apr 2018

I. INTRODUCTION

Progressing towards a sustainable and clean energy future is one of the main challenges of the 21^{st} century. In this context, catalysis plays a key role in the production of chemical energy storage, efficient chemical conversion, and removal of air pollution. Many catalytic devices employ a porous or foam-like structure to maximize the surface and thus maximize the conversion rate. Such structures in turn induce complex mass transport by the gas flow and even more complex heat transport phenomena through the gas and the solid part of the reactor device, where local heat build-up compromises the reactor stability [1–3]. While experimental insight is often not possible at the necessary resolution, computer simulations offer unique and detailed information over a wide range of length and time scales.

Over the last two decades the lattice Boltzmann method (LBM) [4, 5] has become a reliable and fast technique for simulations of complex flows at mesoscopic length scales, such as in many porous materials [6]. In contrast to solving the Navier-Stokes equation, the LBM incorporates microscopic information in form of the single-particle distribution functions as described in the Boltzmann equation, and it is predestined for high performance computer applications due to its straightforward parallalization and its high efficiency. While the traditional LBM is a single component athermal method, several approaches have been suggested to include temperature dynamics [7–11] and extend to simulation of arbitrary gas-mixtures [6, 12–14]. In particular, Kang *et al.* [15, 16] suggested a multicomponent thermal LBM. In this model, each chemical gas component is described through individual distribution functions and relaxation parameters describing the individual transport coefficients (viscosity, thermal and mass diffusivity), where self-consistent correction terms restore the transport equations in the macroscopic limit. Surface chemical reactions can hereby be included through flux boundary conditions in a very flexible way [16, 17]. This approach however mimics isothermal walls. Therefore, it lacks the ability to simulate a heat built-up, and does not allow for heat transport across the solid-gas interface and through the solid. In this paper we develop a multicomponent thermal LBM scheme based on the work of Kang *et al.* and augment it with a finite difference (FD) solver for the heat equation in the solid parts of the simulation domain (e.g. the porous host material), together with a coupling strategy for a novel and consistent treatment of the reaction enthalpy.

The article is structured as follows. In Sec. II the thermal multicomponent lattice Boltzmann model based on Ref. 16 is introduced. In Sec. III the macroscopic mass and energy transport of the model is examined with a Chapman-Enskog analysis. The deviations of the macroscopic transport equation from the kinetic theory of gases differ from those reported in Ref. 16, which consequently leads to different correction terms. A detailed derivation is offered in the supplementary material [18]. We further explain how the relaxation times relate to the viscosity and diffusion coefficient of the individual components. In Sec. IV we give a detailed description of our implementation, further substantiate our correction terms and scrutinize the overall model by benchmarking the mass and thermal diffusivities in the multicomponent system.

* d.berger@fz-juelich.de

We furthermore simulate a thermal Couette flow for a mixture of gases and compare the results to the analytical solution. In Sec. V we present our model to simulate thermal diffusion through a solid-fluid interface by adding a finite difference (FD) solver for the heat equation in the solid. We exemplify our model with an enthalpy consistent simulation of a reactive flow through a packed-cubes model geometry in Sec. VI. The surface of the cubes catalyzes the water-gas-shift reaction, the catalytic reaction of carbon monoxide and water to carbon dioxide and hydrogen. This reaction is of high relevance for the production of highly purified hydrogen gas for application in fuel cells. In Sec. VII we conclude the paper and discuss limitations of the presented model in resolution and parameter space.

II. THERMAL MULTICOMPONENT MODEL

In this section the thermal multicomponent LBM based on the work of Kang *et al.* [15, 16] is introduced to clarify the differences between this work and the original one. We restrict ourselves to the standard D2Q9-lattice (see Fig. 1)[19]. An extension towards the general 3-dimensional case is planned for the future. In the thermal multicomponent LBM the distribution functions f_j of each component j of a mixture of N components is propagated by a kinetic equation involving advection and collision

$$\partial_t f_{ji} + c_{ji\alpha}\partial_\alpha f_{ji} = -\frac{1}{\tau_{1j}}(f_{ji} - f^*_{ji}) - \frac{1}{\tau_{2j}}(f^*_{ji} - f^{eq}_{ji}), \tag{1}$$

where f^{eq}_{ji} is the equilibrium distribution function, f^*_{ji} the distribution function of an auxiliary quasi-equilibrium state and i indices the microscopic velocities $c_{ji\alpha}$, with α being the direction along the x and y axis. On the D2Q9 lattice the microscopic velocities $c_{ji\alpha}$ then read

$$\begin{aligned} c_{jix} &= c_j(0, 1, 0, -1, 0, 1, -1, -1, 1) \\ c_{jiy} &= c_j(0, 0, 1, 0, -1, 1, 1, -1, -1), \end{aligned} \tag{2}$$

which corresponds to a lattice spacing of $\delta x = 1$ and a time step of $\delta t = 1$. In general, each component has a different mass and thus also different microscopic velocities. This manifests in two ways: first, c_{ji} are scaled with a factor $c_j = \sqrt{M_0/M_j}$ (it is convenient to work with relative masses. From hereon we scale all molar masses relative to the mass of the lightest element $M_j \longrightarrow M_j/M_0$). Second, the streaming step is impeded which will be discussed further below. In contrast to the single component LBM the collision operator in Eq. (1) separates into two terms: Based on a fast–slow decomposition along a quasi–equilibrium trajectory [20, 21] the multicomponent Bhatnagar-Gross-Krook [22] collision operator relaxes the distribution towards the mixture equilibrium distribution f^{eq}_{ji} in a two-step process via the auxiliary

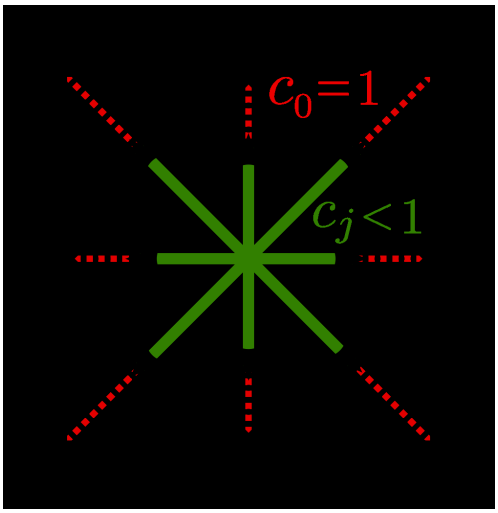


FIG. 1. D2Q9 lattice: only the lightest element with $c_j = 1$ (red) is streamed on-lattice, while all heavier elements are streamed off-lattice with $c_j < 1$ (green).

equilibrium for each component f^*_{ji} as motivated by Arcidiacono *et al.* [14] and Ansumali *et al.* [23]. The physical meaning of the corresponding different relaxation times τ_{1j} and τ_{2j} will be clarified in the next Section.

The relevant moments of the f_{ji}, which are needed for the analysis of the model, are the individual density, momentum, energy, pressure tensor, third order moment, energy flux and the individual fourth order contracted moment:

$$\begin{aligned} \rho_j &= \sum_{i=0}^{8} f_{ji}, \quad J_{j\alpha} = \sum_{i=0}^{8} c_{ji\alpha} f_{ji}, \quad E_j = \sum_{i=0}^{8} c^2_{ji} f_{ji}, \\ P_{j\alpha\beta} &= \sum_{i=0}^{8} c_{ji\alpha} c_{ji\beta} f_{ji}, \quad Q_{j\alpha\beta\gamma} = \sum_{i=0}^{8} c_{ji\alpha} c_{ji\beta} c_{ji\gamma} f_{ji}, \\ q_{j\alpha} &= \sum_{i=0}^{8} c_{ji\alpha} c^2_{ji} f_{ji} \quad R_{j\alpha\beta} = \sum_{i=0}^{8} c_{ji\alpha} c_{ji\beta} c^2_{ji} f_{ji}. \end{aligned} \tag{3}$$

The equilibrium distribution f^{eq}_{ji} function is found from minimizing the H-theorem ($H = \sum_{ji} f_{ji} \ln f_{ji}$) under the constraints of local conservation of the individual density, the mixture momentum, mixture pressure tensor and energy [11, 15, 16]. In the specific case of the D2Q9-lattice f^{eq}_{ji} can be written as

$$\begin{aligned} f^{eq}_{ji} =& \rho_j \prod_{\alpha=x,y} \frac{1 - 2c^2_{0i\alpha}}{2^{c^2_{0i\alpha}}} [(c^2_{0i\alpha} - 1) \\ &+ \sqrt{M_j} c_{0i\alpha} \frac{J_\alpha}{\rho} + M_j \frac{J^2_\alpha}{\rho^2} + T], \end{aligned} \tag{4}$$

where $c_{0i\alpha}$ are the microscopic velocities of the lightest element ($M_0 = 1$). The equilibrium is defined by the individual densities ρ_j and the momentum J_α and the

temperature T of the mixture, which are defined by the total energy of the system:

$$\begin{aligned}\rho &= \sum_j^N \rho_j = \sum_j^N \sum_{i=0}^8 f_{ji},\\ J_\alpha &= \sum_j^N J_{j\alpha} = \sum_j^N \sum_{i=0}^8 c_{ji\alpha} f_{ji},\\ E &= 2CT + \frac{J^2}{\rho} = \sum_j^N E_j = \sum_j^N \sum_{i=0}^8 c_{ji}^2 f_{ji}.\end{aligned} \tag{5}$$

The concentration of the mixture C is the sum of the individual concentrations $C = \sum_j^N C_j$, where $C_j = \rho_j / M_j$.

The distribution of the auxiliary state can be derived in a similar fashion as the f_{ji}^{eq}. In this case an additional constraint is needed for the minimization of the H functional which reflects the quasi-conserved quantity of the quasi-equilibrium state, namely either the difference between individual pressure tensors or the difference between individual mass fluxes [17]. For flow simulations of gas mixtures in porous material, the local mass transport is typically governed by diffusion, i.e. the individual momentum is the variable which only slowly relaxes towards the equilibrium and is thus conserved in the quasi-equilibrium state. In this case the form of f_{ji}^* is very similar to f_{ji}^{eq}, with the difference that the momentum of the mixture is replaced by the individual moments:

$$\begin{aligned}f_{ji}^* =& \rho_j \prod_{\alpha=x,y} \frac{1-2c_{0i\alpha}^2}{2^{c_{0i\alpha}^2}} [(c_{0i\alpha}^2 - 1)\\ &+ \sqrt{M_j} c_{0i\alpha} \frac{J_{j\alpha}}{\rho_j} + M_j \frac{J_{j\alpha}^2}{\rho_j^2} + T]\end{aligned} \tag{6}$$

Note, that for the case that the relaxation towards the equilibrium is governed by viscosity, i.e. the individual pressure difference equilibrate slowly, a different form of f_{ji}^* has to be derived [17].

The moments of the equilibrium distribution recover those from the kinetic theory of gases up to the second order by construction. Deviations however appear for the higher moments, and are labelled $Q'_{j\alpha\beta\gamma}$, $q'_{j\alpha}$ and $R'_{j\alpha\beta}$. These deviation terms stem from the simplicity of the lattice itself. In principle, an equilibrium distribution which also conserves higher moments can be derived for a lattice which includes more velocities [24–26]. This strategy however quickly becomes cumbersome, as e.g. the computation of the pressure tensor scales quadratically with the number of velocities ($\propto \mathcal{O}(N^2)$). Here, we choose an alternative strategy by explicitly calculating the deviation from the macroscopic limits by means of a Chapman-Enskog analysis [27]. The deviation terms can then be corrected for by adding appropriate forcing terms to the kinetic equation of the model, which will be derived in the following.

III. MACROSCOPIC LIMIT

The macroscopic limit of the model can be examined in terms of a Chapman-Enskog analysis, i.e. the distribution function and the time derivative are expanded in orders of the Knudsen number Kn around the equilibrium: $f_{ji} = f_{ji}^{eq} + Kn\ f_{ji}^{(1)}$ and $\partial_t = \partial_t^{(0)} + Kn\ \partial_t^{(1)}$. The kinetic equation (Eq. (1)) together with the definition of the moments (Eq. (3)) and the equilibrium and auxiliary equilibrium distribution determine the transport equations and allow to relate the characteristic relaxation times τ_{1j} and τ_{2j} to the corresponding physical properties of the gas mixture. The to–be–conserved quantities of interest are the total density, the momentum and the energy, as summarized in the transport equations

$$\begin{aligned}\partial_t \rho + \partial_\alpha J_\alpha = 0, \quad \partial_t J_\alpha + \partial_\beta P_{\alpha\beta} = 0,\\ \partial_t E + \partial_\alpha q_\alpha = 0.\end{aligned} \tag{7}$$

The quantities of the mixture are only conserved when the moments of the individual species are in agreement with the kinetic theory of gases. Evaluating Eq. (1) for the corresponding individual moments yields the transport equations for the individual density

$$\partial_t \rho_j + \partial_\alpha J_{j\alpha} = 0, \tag{8}$$

the individual momentum

$$\partial_t J_{j\alpha} + \partial_\beta P_{j\alpha\beta} = -\frac{1}{\tau_{j2}} \left(J_{j\alpha} - \frac{\rho_j}{\rho} J_\alpha \right) = -\frac{V_{j\alpha}}{\tau_{j2}}, \tag{9}$$

defining the diffusion flux $V_{j\alpha}$ for the individual species, the individual pressure tensor

$$\begin{aligned}\partial_t P_{j\alpha\beta} + \partial_\gamma Q_{j\alpha\beta\gamma} =\\ -\frac{1}{\tau_{j1}}(P_{j\alpha\beta} - P_{j\alpha\beta}^*) - \frac{1}{\tau_{j2}}(P_{j\alpha\beta}^* - P_{j\alpha\beta}^{eq}),\end{aligned} \tag{10}$$

and the individual energy flux

$$\begin{aligned}\partial_t q_{j\alpha} + \partial_\beta R_{j\alpha\beta} =\\ -\frac{1}{\tau_{j1}}(q_{j\alpha} - q_{j\alpha}^*) - \frac{1}{\tau_{j2}}(q_{j\alpha}^* - q_{j\alpha}^{eq}).\end{aligned} \tag{11}$$

Expansion in terms of the Knudsen number around the equilibrium yields the following first-order expressions for the diffusive flux $V_{j\alpha}$, and the individual pressure tensor and energy flux:

$$\begin{aligned}V_{j\alpha} &= V_{j\alpha}^{eq} + Kn\ V_{j\alpha}^{(1)} = Kn\ V_{j\alpha}^{(1)}\\ P_{j\alpha\beta} &= P_{j\alpha\beta}^{eq} + Kn\ P_{j\alpha\beta}^{(1)}\\ q_{j\alpha} &= q_{j\alpha}^{eq} + Kn\ q_{j\alpha}^{(1)}\end{aligned} \tag{12}$$

In equilibrium the diffusive flux vanishes by definition. After some algebraic transformations (see supplementary material (Ref. [18]) for details) similar expressions can be

found for the individual pressure tensor and the energy flux of the auxiliary state:

$$\begin{aligned} P^*_{j\alpha\beta} &= P^{eq}_{j\alpha\beta} + Kn\left(\frac{J_\alpha}{\rho}V^{(1)}_{j\beta} + \frac{J_\beta}{\rho}V^{(1)}_{j\alpha}\right) \\ q^*_{j\alpha} &= q^{eq}_{j\alpha} + Kn\left(V^{(1)}_{j\alpha}\frac{J^2}{\rho^2} + 2\frac{J_\alpha J_\gamma}{\rho^2}V^{(1)}_{j\gamma} + V^{(1)}_{j\alpha}\frac{4T}{M_j}\right. \\ &\qquad \left. + \frac{1-3T}{M_j}V^{(1)}_{j\alpha} - 3\frac{J^2_\alpha}{\rho^2}V^{(1)}_{j\alpha}\right) \end{aligned} \tag{13}$$

Inserting Eqs. (12) & (13) into the transport equations of the individual moments allows to identify the zeroth-order transport equation of the non-conserved moments:

$$\partial^{(0)}_t J^{eq}_{j\alpha} + \partial_\beta P^{eq}_{j\alpha\beta} = -\frac{V^{(1)}_{j\alpha}}{\tau_{j2}} \tag{14}$$

$$\begin{aligned} &\partial^{(0)}_t P^{eq}_{j\alpha\beta} + \partial_\gamma Q^{eq}_{j\alpha\beta\gamma} = \\ &\quad = -\frac{1}{\tau_{j1}}P^{(1)}_{j\alpha\beta} + \left(\frac{1}{\tau_{j1}} - \frac{1}{\tau_{j2}}\right)\left(\frac{J_\alpha}{\rho}V^{(1)}_{j\beta} + \frac{J_\beta}{\rho}V^{(1)}_{j\alpha}\right) \end{aligned} \tag{15}$$

$$\begin{aligned} \partial^{(0)}_t q^{eq}_{j\alpha} + \partial_\beta R^{eq}_{j\alpha\beta} &= -\frac{1}{\tau_{j1}}q^{(1)}_{j\alpha} + \left(\frac{1}{\tau_{j1}} - \frac{1}{\tau_{j2}}\right)V^{(1)}_{j\alpha}\frac{4T}{M_j} \\ &+ \left(\frac{1}{\tau_{j1}} - \frac{1}{\tau_{j2}}\right)V^{(1)}_{j\alpha}\left(\frac{J^2}{\rho^2} + \frac{1-3T}{M_j} - 3\frac{J^2_\alpha}{\rho^2}\right) \\ &+ \left(\frac{1}{\tau_{j1}} - \frac{1}{\tau_{j2}}\right)V^{(1)}_{j\gamma}2\frac{J_\alpha J_\gamma}{\rho^2} \end{aligned} \tag{16}$$

Note that Eq. (16) deviates from the terms given in the previous work of Kang *et al.* [16]. The detailed derivation can be found in the supplementary material to this work [18]. In the following, Eqs. (14–16) are further analyzed to examine the macroscopic limits of the kinetic model.

A. Mass diffusivity

The mass diffusivity is described by the transport equation of the individual moments Eq. (14). An expression for the first-order diffusive flux $V^{(1)}_{j\alpha}$ can be found by solving Eq. (14) for $V^{(1)}_{j\alpha}$ and using the zeroth-order transport equation for the conserved moments together with the identity $J^{eq}_{j\alpha} = Y_j J^{eq}_\alpha$:

$$V^{(1)}_{j\alpha} = \tau_{j2}\Big[Y_j\partial_\alpha(CT) - \partial_\alpha(C_jT)\Big], \tag{17}$$

where we introduced the mass fraction $Y_j = \rho_j/\rho$.

Together with the first expression of Eq. (12) and the definition of the diffusion flux in (Eq. (9)), Eq. (17) can be rewritten in a form which resembles the Maxwell-Stefan diffusion equation

$$\partial_\alpha X_j = -\frac{V_{j\alpha}}{p\tau_{j2}} + \frac{Y_j - X_j}{p}\partial_\alpha p, \tag{18}$$

where we introduced the molar fraction $X_j = C_j/C$, and the definition of the pressure $p = CT$. This allows to read off an expression

$$\tau_{j2} = \sum_{\substack{k=1\\ j\neq k}}^{N} \frac{\frac{\rho_k\rho_j}{\rho}\left(\frac{J_{k\alpha}}{\rho_k} - \frac{J_{j\alpha}}{\rho_j}\right)}{p\frac{X_jX_k}{D_{jk}}\left(\frac{J_{k\alpha}}{\rho_k} - \frac{J_{j\alpha}}{\rho_j}\right)}, \tag{19}$$

which relates the relaxation time τ_{j2} to the binary diffusion coefficients D_{jk}. This expression is exact, however impractical to use in a lattice Boltzmann simulation; as it depends on the local flow velocities and directions the exact form is expensive to compute. A common approximation [14, 28] is to assume that the term $\frac{J_{k\alpha}}{\rho_k} - \frac{J_{j\alpha}}{\rho_j}$ is of the same order for all pairs of species, or — in other words — to employ mass-averaged diffusion velocities. With this assumption, Eq. (19) reduces to

$$\tau_{j2} = \frac{\rho_j}{X_j p}D_j, \tag{20}$$

with

$$D_j = \frac{1-Y_j}{\sum_{\substack{k=1\\ j\neq k}}^{N}\frac{X_k}{D_{jk}}} \tag{21}$$

being the mixture averaged diffusion coefficient of species j. This approximation of mass-averaged diffusion velocities impairs the total momentum conservation

$$\partial_t J_\alpha + \partial_\beta P_{\alpha\beta} = -\sum_j \frac{V_{j\alpha}}{\tau_{j2}} = -\sum_j \frac{1}{\tau_{j2}}\left(J_{j\alpha} - \frac{\rho_j}{\rho}J_\alpha\right), \tag{22}$$

where the terms on the right hand side generally do not add up to zero, and hence act as a spurious force on the gas-mixture. We restore the total momentum conservation by adding a corrective diffusion velocity U^c_α [29, 30] to the individual mass flux

$$J_{j\alpha} = \widetilde{J}_{j\alpha} + \rho_j U^c_\alpha, \tag{23}$$

where $\widetilde{J}_{j\alpha}$ is the uncorrected momentum of species j. This technique has also been applied in previous multicomponent lattice Boltzmann approaches [14, 16]. Inserting Eq. (23) into Eq. (22) yields a final expression for the corrective diffusion velocity

$$U^c_\alpha = \frac{\sum_j \frac{1}{\tau_{j2}}\left(\widetilde{J}_{j\alpha} - \frac{\rho_j}{\rho}J_\alpha\right)}{\sum_j \frac{1}{\tau_{j2}}\rho_j}. \tag{24}$$

This corrective velocity is then added to the kinetic equation (Eq. (1)) using a forcing term

$$\Psi_{ji}^{(I)} = \psi_{ji\alpha}\frac{\rho_j U_\alpha^c}{\tau_{j2}}, \tag{25}$$

where the matrix coefficient $\psi_{ji\alpha}$ is chosen in a way that $\Psi_{ji}^{(I)}$ solely affects the momentum equation:

$$\begin{aligned}\psi_{jix} &= \frac{1}{4c_j}\{0,4,0,-4,0,-1,1,1,-1\}\\ \psi_{jiy} &= \frac{1}{4c_j}\{0,0,4,0,-4,-1,-1,1,1\}\end{aligned} \tag{26}$$

The velocity correction discussed above is only a first-order approximation to the exact solution. Higher orders were discussed e.g. by Oran and Boris [29], but go beyond the scope of this implementation.

B. Viscosity

The viscosity of the mixture μ (and the individual viscosities μ_j) and its relation to the relaxation times τ_{1j} can be determined by examining the macroscopic mass transport equation of the mixture as

$$\begin{aligned}\partial_t J_\alpha &= \partial_t^{(0)} J_\alpha + \sum_j \tau_{j1}\partial_t^{(1)} J_{j\alpha}\\ &= -\partial_\beta P_{\alpha\beta}^{eq} - \sum_j \partial_\beta P_{j\alpha\beta}^{(1)}.\end{aligned} \tag{27}$$

The first-order pressure tensor is computed from Eq. (15), which can be split into two parts,

$$P_{j\alpha\beta}^{(1)} = P_{j\alpha\beta}^{neq} + P_{j\alpha\beta}^{''}. \tag{28}$$

The first term is the desired nonequilibrium pressure tensor as known from the kinetic theory of gases:

$$P_{j\alpha\beta}^{neq} = -\tau_{j1}C_j T\partial_\gamma\left(\frac{J_\alpha}{\rho}\delta_{\beta\gamma} + \frac{J_\beta}{\rho}\delta_{\alpha\gamma} - \frac{J_\gamma}{\rho}\delta_{\alpha\beta}\right) \tag{29}$$

All deviations from the nonequilibrium pressure tensor are shifted into the second term as

$$\begin{aligned}P_{j\alpha\beta}^{''} =& -\tau_{j1}\partial_\gamma Q'_{j\alpha\beta\gamma} + \frac{\tau_{j1}X_j}{2}\partial_\gamma q'_\gamma\delta_{\alpha\beta}\\ &+\left[\left(\frac{J_\alpha}{\rho}\right)V_{j\beta}^{(1)} + \left(\frac{J_\beta}{\rho}\right)V_{j\alpha}^{(1)}\right].\end{aligned} \tag{30}$$

These terms involve the aforementioned deviations from the third-order and contracted third-order moment of the equilibrium distribution. The explicit form together with a detailed derivation can be found in the supplementary material [18].

The mass transport equation of the mixture can finally be written as

$$\begin{aligned}&\partial_t J_\alpha + \partial_\alpha(CT) + \partial_\beta\Bigg[\frac{J_\alpha j_\beta}{\rho} - \sum_j^N(\tau_{j1}C_j T)\\ &\times\partial_\gamma\left(\frac{J_\alpha}{\rho}\delta_{\beta\gamma} + \frac{J_\beta}{\rho}\delta_{\alpha\gamma} - \frac{J_\gamma}{\rho}\delta_{\alpha\beta}\right)\Bigg] = -\sum_j \partial_\beta P_{j\alpha\beta}^{''},\end{aligned} \tag{31}$$

where the right hand side of the equation constitutes the deviation from the kinetic theory of gases. Similar to the deviation term in Eq. (22) this term can, however, be removed by adding a forcing term

$$\Psi_{ji}^{(II)} = \psi_{ji\alpha}\partial_\beta P_{j\alpha\beta}^{''} \tag{32}$$

to the kinetic equation, where again the coefficients $\psi_{ji\alpha}$ ensure that Eq. (32) only affects the momentum equation (and not the density or energy). The total correction term for the momentum now reads

$$\Psi_{ji} = \Psi_{ji}^{(I)} + \psi_{ji\alpha}\partial_\beta P_{j\alpha\beta}^{''}. \tag{33}$$

Note that the individual deviation terms $\partial_\beta P_{j\alpha\beta}^{''}$ define the correction term for each species, rather than the total deviation term $\partial_\beta P_{\alpha\beta}^{''} = \sum_j \partial_\beta P_{j\alpha\beta}^{''}$. This is in disagreement with the previous multicomponent thermal model by Kang *et al.* It can however easily be tested that the indifferentiability principle (a mixture of two identical gases should coincide with a single component simulation [11]) is only fulfilled by the expression given in Eq. 33.

Comparing Eq. (31) to the kinetic theory of gases allows to determine the dynamic viscosity of the mixture as

$$\mu = \sum_j^N(\tau_{j1}C_j T). \tag{34}$$

There is no trivial way to express the viscosity of a mixture by the viscosity of the individual species μ_j. We use the empirical formula by Wilke [31, 32] and express the viscosity of the mixture by the viscosities, molar fractions and molar weights of the individual components,

$$\mu = \sum_j^N \frac{X_j\mu_j}{\sum_k^N X_k\varphi_{jk}}, \tag{35}$$

with

$$\varphi_{jk} = \frac{1}{\sqrt{8}}\frac{1}{\sqrt{1+\frac{M_j}{M_k}}}\left[1+\left(\frac{\mu_j}{\mu_k}\right)^{1/2}\left(\frac{M_k}{M_j}\right)^{1/4}\right]. \tag{36}$$

Combining Eq. (34) and the Wilke formula allows to express the relaxation times τ_{j1} as a function of the individual dynamic viscosities, molar fractions and molar masses as

$$\tau_{j1} = \frac{\mu_j}{CT\sum_k^N X_k\varphi_{jk}}. \tag{37}$$

C. Heat conductivity

For a consistent thermal model also the third macroscopic transport equation in Eq. (7), the energy transport, needs to restore the correct behaviour known from the kinetic theory of gases. In a similar fashion to Sec. III B the zeroth- and first-order of the energy transport of the mixture have to be combined:

$$\begin{aligned}\partial_t E &= \partial_t^{(0)} E + \sum_j \tau_{j1} \partial_t^{(1)} E_j \\ &= -\partial_\alpha q_\alpha^{eq} - \sum_j \partial_\alpha q_{j\alpha}^{(1)}\end{aligned} \tag{38}$$

In contrast to the mass transport equation already the equilibrium energy flux deviates from the desired Maxwell-Boltzmann (MB) form ($q_\alpha^{eq} = q_\alpha^{MB} + q'_\alpha$). The individual first-order terms $q_{j\alpha}^{(1)}$ can be computed from Eq. (16) as

$$q_{j\alpha}^{(1)} = q_{j\alpha}^{neq} + q''_{j\alpha}, \tag{39}$$

which again separates into the desired nonequilibrium energy flux $q_{j\alpha}^{neq}$ and a deviation term $q''_{j\alpha}$. The nonequilibrium term is then derived as

$$q_\alpha^{neq} = -\sum_j \left[4\tau_{j1} \frac{C_j T}{M_j} \partial_\alpha T - 4T \frac{1}{M_j} V_{j\alpha}^{(1)} \right] + 2\frac{J_\beta}{\rho} P_{\alpha\beta}^{(neq)}. \tag{40}$$

Note that the signs in front of the second and third term deviate from the expression given in the thermal multicomponent model by Kang *et al.* [16]. For the case of a single component ($N = 1$) Eq. (40) simplifies to the nonequilibrium energy flux of the single component thermal LBM of Prasianakis and Karlin [11]. In order to prove that Eq. (40) is correct the full derivation is given in the supplementary material of this work [18].

From Eq. (40) and Eq. (38) the macroscopic energy equation can be written down in terms of the time-evolution of the temperature field in the bare model (without correction terms):

$$\begin{aligned}\partial_t T =& \ \partial_t^{(0)} T + \partial_t^{(1)} T \\ =& -\frac{J_\alpha}{\rho}\partial_\alpha T - T\partial_\alpha\left(\frac{J_\alpha}{\rho}\right) + \frac{1}{C}\partial_\alpha\left(\sum_j 2\tau_{j1}\frac{C_j T}{M_j}\partial_\alpha T\right) \\ &- \frac{1}{C}\partial_\alpha\left(\sum_j 2T\frac{1}{M_j}V_{j\alpha}^{(1)}\right) + \frac{1}{C}\sum_j \tau_{j1}(C_j T)\partial_\alpha\left(\frac{J_\beta}{\rho}\right) \\ &\times\left[\partial_\alpha\left(\frac{J_\beta}{\rho}\right) + \partial_\beta\left(\frac{J_\alpha}{\rho}\right) - \delta_{\alpha\beta}\partial_\gamma\left(\frac{J_\gamma}{\rho}\right)\right] \\ &- \frac{1}{2C}\left(\partial_\alpha q'_\alpha + \partial_\alpha q''_\alpha\right) + \frac{1}{C}\frac{J_\alpha}{\rho}\partial_\beta P''_{\alpha\beta} \quad ,\end{aligned} \tag{41}$$

where we use $q'_\alpha = \sum_j q'_{j\alpha}$ and $q''_\alpha = \sum_j q''_{j\alpha}$. A detailed derivation is offered in the supplementary material. Note that the last term is not mentioned in the previous work by Kang *et al.*, although it is present in the bare model Eq. (1). This term is however already compensated by employing the forcing term $\Psi_{ji}^{(II)}$. The deviation term $q''_{j\alpha}$ (see supplementary material) leads to a spuriously low thermal conductivity of the bare thermal multicomponent model and ruins the energy conservation. It can be removed from the energy equation by adding a third forcing term

$$\Phi_{ji} = \phi_{ji}(\partial_\alpha q'_{j\alpha} + \partial_\alpha q''_{j\alpha}), \tag{42}$$

to the kinetic equation, where the coefficients

$$\phi_{ji} = \frac{1}{8c_j^2}\{-12, 4, 4, 4, 4, -1, -1, -1, -1\} \tag{43}$$

ensure that Φ_{ji} only affects the energy equation ($\sum_i \phi_{ji} = 0$, $\sum_i c_{ji}\phi_{ji} = 0$). Again, we shall highlight the fact that the individual deviation terms $\partial_\alpha q'_{j\alpha}$ and $\partial_\alpha q''_{j\alpha}$ define the correction term for each species, rather than the total deviation term. This again is in disagreement with the multicomponent thermal model by Kang *et al.*. It can however easily be shown that the indifferentiability principle is only fulfilled by Eq. (42).

When comparing Eq. (41) to the temperature transport equation of the kinetic theory of gases, the thermal conductivity of the mixture is determined as

$$\kappa = \bar{M}\sum_j 2\tau_{j1}\frac{C_j T}{M_j}, \tag{44}$$

with $\bar{M}$ being the average mass [33].

One important measure of a gas is its ratio between viscous and thermal diffusivity, which is known as the Prandtl number (Pr). The thermal LBM can be easily extended to specifically adjust the Prandtl number Pr of the mixture. In case the deviation term $q''_{j\alpha}$ is properly compensated through Eq. (42) it is given by

$$Pr = \frac{c_p \mu}{\kappa} = \frac{c_p \sum_j \tau_{j1} C_j}{\bar{M}\sum_j \tau_{j1}\frac{C_j}{M_j}}, \tag{45}$$

where c_p is the isobaric specific heat capacity.

Similar to Ref. 11 a variable Prandtl number can be introduced by adding another force term

$$\Phi_{ji}^{Pr} = \phi_{ji}\partial_\alpha q_{j\alpha}^{Pr}, \tag{46}$$

to the kinetic equation, where

$$q_{j\alpha}^{Pr} = \left(\frac{2c_p}{Pr} - \frac{4}{M_j}\right)\tau_{1j} C_j T \partial_\alpha T \tag{47}$$

is ensured to only act on the energy equation through the coefficients ϕ_{ji}. The second term compensates the first term of the the nonequilibrium energy flux (Eq. (40)), while the first term sets the thermal conductivity to

$$\kappa^{Pr} = \frac{c_p \sum_j \tau_{j1} C_j T}{Pr} \ . \tag{48}$$

Further extensions in which the Prandtl number can be adjusted for each species separately are possible [16].

IV. IMPLEMENTATION

A. Corrected LBM

In order to achieve that the macroscopic mass and energy transport is in agreement with the kinetic theory of gases, the correction terms derived in the previous section need to be added to the kinetic equation

$$\partial_t f_{ji} + c_{ji\alpha}\partial_\alpha f_{ji} = -\frac{1}{\tau_{1j}}(f_{ji} - f^*_{ji}) - \frac{1}{\tau_{2j}}(f^*_{ji} - f^{eq}_{ji}) + \Psi_{ji} + \Phi_{ji}. \tag{49}$$

Eq. (49) is now the kinetic equation for a thermal flow of a general gas mixture, which conserves momentum and energy. This equation is to be integrated in time from t to $t+\delta t$. In order to avoid implicitness the distributions f_{ji} are transformed in standard fashion to

$$g_{ji} = f_{ji} + \frac{\delta t}{2\tau_{1j}}(f_{ji} - f^*_{ji}) + \frac{\delta t}{2\tau_{2j}}(f^*_{ji} - f^{eq}_{ji}) - \frac{\delta t}{2}(\Psi_{ji} + \Phi_{ji}). \tag{50}$$

as done in previous approaches [7, 11, 14, 16, 23]. Time integration through the trapezoidal rule yields the equation

$$\begin{aligned} g_{ji}(t+\delta t) =& g_{ji}(t) - \frac{2\delta t}{\delta t + 2\tau_{1j}}[g_{ji}(t) - f^*_{ji}(t)] \\ &- \frac{2\delta t}{\delta t + 2\tau_{1j}}\frac{\tau_{j1}}{\tau_{j2}}[f^*_{ji}(t) - f^{eq}_{ji}(t)] \\ &+ \frac{2\delta t\tau_{j1}}{\delta t + 2\tau_{1j}}[\Psi_{ji}(t) + \Phi_{ji}(t)], \end{aligned} \tag{51}$$

which relates the pre-collision population $g_{ji}(t)$ to the post-collision population $g_{ji}(t+\delta t)$. The functions f^*_{ji}, f^{eq}_{ji}, Φ_{ji} and Ψ_{ji} require the moments of the distribution function f_{ji} (Eq. (3)). We can, however, calculate the relevant moments of f_{ji} from the populations g_{ji} following the instructions in [16, 23]:

$$\begin{aligned} \rho_j(f) &= \rho_j(g) = \sum_i g_{ji}, \\ J_{j\alpha}(f) &= \frac{J_{j\alpha}(g) + \frac{\delta t}{2\tau_{j2}}J_{j\alpha}(f^{eq}) + \frac{\delta t}{2}\sum_i c_{ji\alpha}\Psi_{ji}}{1 + \frac{\delta t}{2\tau_{j2}}}, \\ &= \frac{\sum_i c_{ji\alpha}g_{ji} + \frac{\delta t}{2\tau_{j2}}\sum_i c_{ji\alpha}f^{eq}_{ji} + \frac{\delta t}{2}\sum_i c_{ji\alpha}\Psi_{ji}}{1 + \frac{\delta t}{2\tau_{j2}}}, \\ T(f) &= \frac{1}{2C}\left[E(g) - \frac{(J(g))^2}{\rho}\right] + \frac{\delta t}{4C}\sum_j\sum_i c^2_{ji}\Phi_{ji}. \end{aligned} \tag{52}$$

This, of course, has the immediate advantage that the populations f_{ji} are no longer needed during the simulations, and transformations between f_{ji} and g_{ji} can be avoided.



FIG. 2. Illustration of streaming step for a heavier component with $c_j < 1$ mapping the population $g\big|^{on}_x \longrightarrow g\big|^{off}_{x+1}$ onto an off-lattice position, labelled by a superscript *off*. A central difference interpolation scheme is used for all nodes except for wall nodes A and Z, where a forward/backward scheme has to be used instead.

The correction terms Φ and Ψ involve the calculation of gradients, which are all obtained through a second-order finite difference scheme.

The relaxation times τ_{1j} and τ_{2j} are defined via the viscosities and the binary diffusion coefficient of each component in the gas mixture. These values can be calculated from tabulated Lennard-Jones parameters of the idealized gas [32] and the local partial pressures and temperature of the gas mixture [16]. To capture the full dynamics in a consistent way, the relaxation times need to be updated in each iteration and at each lattice site as the local conditions change over time.

B. Interpolation

In a general mixture different species have different masses and thus also different microscopic velocities c_{ji}. This complicates the streaming step as the propagated distance within one time step is different for each species. Fig. 2 illustrates the streaming for the velocities $c_j < 1$, where the propagation distance during one time step is $\delta x = \|c_j\|\delta t < 1$. Starting from an on-lattice position (labelled with a capital letter), the populations $g\big|^{on}_x$ are streamed onto an off-lattice position $g\big|^{off}_{x+1}$. Models employing multiple lattices (a lattice for every species) are possible. This, however, only shifts the difficulty into the collision step with widely unknown accuracy.

Here, we choose to work with a single lattice, which hosts the lightest gas species exactly. All heavier species are interpolated according to an upwind interpolation scheme suggested by Arcidiacono *et al.* [17], with the difference that here the transformed populations g_{ji} (and not f_{ji}) are interpolated:

$$\begin{aligned} g_{ji}\big|^{on}_x = g_{ji}\big|^{off}_x + g'_{ji}\big|^{off}_x(1 - \|c_j\|\delta t) \\ + g''_{ji}\big|^{off}_x\frac{1}{2}(1 - \|c_j\|\delta t)^2. \end{aligned} \tag{53}$$

The first g'_{ji} and second derivatives g''_{ji} are calculated from second-order central finite differences of neighboring off-lattice populations

$$\begin{aligned} g'_{ji}\big|^{off}_x &= \frac{g_{ji}\big|^{off}_{x+1} - g_{ji}\big|^{off}_{x-1}}{2} \\ g''_{ji}\big|^{off}_x &= g_{ji}\big|^{off}_{x+1} - 2\cdot g_{ji}\big|^{off}_x + g_{ji}\big|^{off}_{x-1}. \end{aligned} \tag{54}$$

Fig. 2 illustrates the interpolation step for the streaming along lattice direction $i = 1$ with the fluid domain between two walls positioned at lattice node A and Z. For the bulk fluid domain Eq. (54) is used to calculate the first and second derivatives. Close to the wall, however, e.g. at lattice site B where A is a wall node and A^{off} does not exist, the first and second derivatives are approximated through second-order forward finite differences

$$\begin{aligned} g'_{ji}|_B^{off} &= \frac{4g_{ji}|_C^{off} - g_{ji}|_D^{off} - 3g_{ji}|_B^{off}}{2} \\ g''_{ji}|_B^{off} &= -2g_{ji}|_C^{off} + g_{ji}|_D^{off} + g_{ji}|_B^{off}. \end{aligned} \tag{55}$$

Respectively, interpolation onto a wall where $g_{ji}|_{x+1}^{off}$ does not exist, e.g. at the wall node Z in Fig. 2, we get

$$\begin{aligned} g'_{ji}|_Z^{off} &= -\frac{4g_{ji}|_Y^{off} - g_{ji}|_X^{off} - 3g_{ji}|_Z^{off}}{2} \\ g''_{ji}|_Z^{off} &= -2g_{ji}|_Y^{off} + g_{ji}|_X^{off} + g_{ji}|_Z^{off}. \end{aligned} \tag{56}$$

Note that the negative sign in the upper formula of Eq. (56) aligns the first derivative with the direction of interpolation, while the second derivative is symmetric. Eqs. (55) and (56) are approximations to the exact derivatives, which induces an error to the overall mass conservation. This error correlates with the net flux perpendicular to the wall and with the density gradients. In long simulations with periodic boundary conditions around the simulation box this potentially becomes an issue. In practice, interpolated species can easily be replenished though appropriate inlet boundary conditions, as exemplified in Sec. VI

C. Reactive boundary conditions

Surface chemical reactions are simulated through appropriate boundary conditions at the gas-solid interface. This can be done by modifying the individual mass flux balance perpendicular to the wall by a reaction term S_j

$$J_j^{out} - J_j^{in} = S_j, \tag{57}$$

where J_j^{out} denotes the mass flux towards the wall, respectively J_j^{in} is the mass flux pointing back into the gas domain. J_j^{out} and J_j^{in} can be expressed by the distribution function as

$$J_j^{out} = \sum_{\{i|c_{ji\alpha}n_\alpha<0\}} |c_{ji\alpha}n_\alpha| f_{ji}, \tag{58}$$

where the sum is restricted to values of i such that the projection of $c_{ji\alpha}$ onto the surface normal n_α is negative (see Figure 3). Analogously,

$$J_j^{in} = \sum_{\{i|c_{ji\alpha}n_\alpha>0\}} |c_{ji\alpha}n_\alpha| f_{ji}. \tag{59}$$

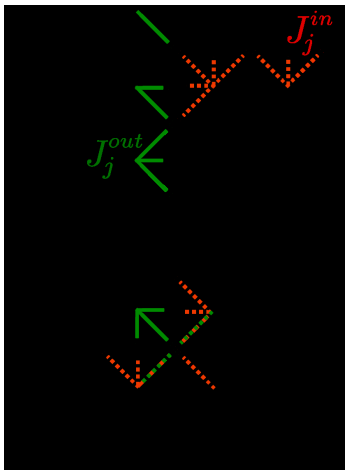


FIG. 3. Illustration of the boundary conditions at the wall: the outflowing populations (green) thermalize and react on the wall nodes (black line). The unknown inflowing populations (red) are calculated from Eq. (61). Around concave corner sites populations act as outflowing and inflowing populations at the same time (red-green dashed).

Various schemes exist in the literature to incorporate boundary conditions on the basis of the mass flux. Many of these schemes generalize athermal boundary conditions e.g. the bounce back scheme [34–36]. In many applications it is desirable to simulate a heated catalyst surface, i.e. to include a wall temperature T_w as a parameter of the simulation. One elegant way to achieve this flexibility is to adopt diffusive boundary conditions [17, 37–39]. Diffusive boundary conditions assume that populations at the wall have enough time to thermalize to equilibrium defined by the wall temperature and can thus be written as

$$f_{ji} = f_{ji}^w(\rho_w, U_w, T_w) = \rho_w f_{ji}^{eq}(\mathbb{1}, U_w, T_w), \tag{60}$$

where ρ_w is the density at the wall, and U_w denotes a possible slip velocity at the wall. By further assuming that the correction terms (Φ and Ψ) at the wall can be neglected, the populations f_{ji} can be replaced with the transformed g_{ji} in Eq. (58) and Eq. (59). Together with Eq. (57), the unknown inflowing populations are then given by

$$g_{ji} = f_{ji}^w \frac{\sum_{\{i|c_{ji\alpha}n_\alpha<0\}} |c_{ji\alpha}n_\alpha| g_{ji} + S_j}{\sum_{\{i|c_{ji\alpha}n_\alpha>0\}} |c_{ji\alpha}n_\alpha| f_{ji}^w}. \tag{61}$$

Boundary conditions are implemented such that the wall is positioned on the solid node (black line in Figure 3). The reaction term S_j is a function of the local density at the wall ρ_w. Similar to the procedure described in Ref. 17 ρ_w is determined iteratively: initially, ρ_w is set to the value of the first fluid node. By evaluating the reaction term with the help of Eq. (57), the unknown populations in Eq. (61) can be computed. The result is then used to evaluate a new density by solving Eq. (60)

for ρ_w. This process is iterated until ρ_w is converged (within 10^{-8}). With the converged value of ρ_w, the final unknown populations at the wall are computed from Eq. (61) and stored for further operations. The computation then proceeds with the collision step for all fluid nodes.

It is also possible to mimic a wall mid-grid between the first fluid node and the wall node. This, however, requires an additional interpolation step as described in Ref. 17.

Applying the boundary conditions to arbitrary geometries consisting of plane wall nodes and concave and convex corners is in principle straightforward. The calculated outflowing and inflowing mass flux thereby only differ by the number of populations entering Eq. (61), as illustrated in Figure 3. We, however, need to point out that the interpolation of the streaming step around concave corner sites is problematic. For populations streaming from wall to wall (red-green dashed arrows in Fig. 3) neighboring populations in streaming direction are missing on both sides. This prohibits any interpolation which in turn leads to artificially large mass fluxes in these directions. In this work we restrict the surface geometry to be constructed from planar and convex corner nodes, where such issues do not occur.

The surface chemical reaction not only changes the chemical composition but in general also the temperature of the system according to the reaction enthalpy ΔH_r,

$$\Delta T = \frac{\Delta H_r}{c_p}, \tag{62}$$

where c_p is the isobaric heat capacity.

Previous thermal LBM approaches use the concept of isothermal walls [16], which reflects adiabatic coupling to an infinite bath or solid nodes with infinite heat capacity. For many applications involving chemical reactions it is desirable to capture heat accumulation at the reactor surface and in the reactor volume. This requires to solve the heat equation in the solid nodes, together with a coupling between the solid and the fluid domains. In the following we suggest a simple and efficient way to do that.

D. Benchmarking mass and thermal diffusion

To show the quality of the corrected model the macroscopic mass and energy transport of the LB simulation are benchmarked against analytical solutions. All simulations are done with a gas mixture of H_2, H_2O, CO & CO_2. This yields a maximum ratio of molar masses of 22, which scrutinizes the robustness of the interpolation scheme described in the previous section.

To test the correct mass diffusion a quasi infinite one-dimensional system is set up with two half-spaces with adjugate initial molar fraction, e.g. the molar fraction of CO_2 for $x < 0$ is $X^L_{CO_2} = 0.4$, respectively $X^R_{CO_2} = 0.1$ for $x > 0$, at time $t = 0$. The gradients of molar fractions

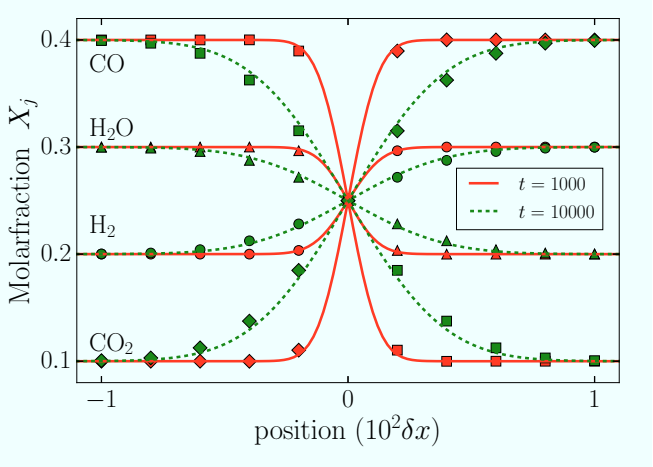


FIG. 4. Mass diffusion of the multicomponent mixture: comparison of molar fractions of the four different species from the LB simulation (symbols) with the analytical solution (lines), at time t=1000 (green) and t=10000 (red).

lead to a diffusion flux according to Fick's law with an analytical solution as a function of time and space given by

$$X_j(x,t) = X_j^L + (X_j^L - X_j^R)\,\mathrm{erf}(\frac{x}{2\sqrt{D_j t}}). \tag{63}$$

The mixture averaged diffusion coefficients D_j are calculated consistently from Eq. (21), the Lennard-Jones parameters of the idealized gas (see Appendix A) and the applied simulation conditions, namely a pressure of 1 bar and a temperature of 293 K. As can be seen from Fig. 4 the simulation results show an excellent agreement with the analytical solution for all four chemical species.

The macroscopic heat transport of the gas mixture is tested by simulating the heat conduction between two isothermal infinite plates with different temperatures of $T_c = 293$ K and $T_h = T_c + \Delta T = 303$ K. Between the two plates a gas mixture of H_2, H_2O, CO & CO_2 with the molar fractions of 20%, 30%, 10% and 40% at 1 bar and 293 K is placed. The system is discretized by 300 lattice sites between the plates, resembling a distance of $L = 100$ μm. Together with a Prandtl number $Pr_j = 0.7$ for each species, the mixture averaged thermal diffusivity ($\alpha = \kappa/2C$) is calculated from the thermal conductivity κ and the concentration C as $\alpha = 0.085$ (in LB units, see Appendix B). Diffusive boundary conditions [37, 38] are applied to both walls in the x-direction, and periodic boundary conditions in the y-direction, respectively. The resulting temperature profiles (Fig. 5) show excellent agreement with the analytical solution of the heat equation given by

$$T(x,t) = T_0 + \Delta T\left[1 - \mathrm{erf}\left(\frac{x}{2\sqrt{\alpha t}}\right)\right]. \tag{64}$$

Finally, the viscous heat dissipation is tested in terms of a thermal Couette flow. Similar to the previous test

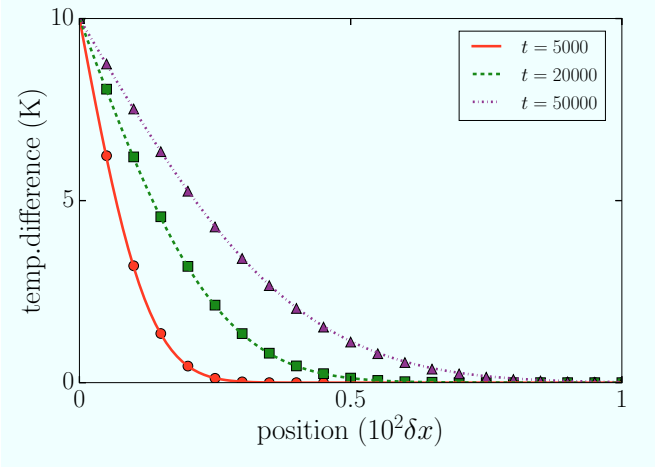


FIG. 5. Thermal diffusivity in the multicomponent mixture between two parallel plates: comparison of the temperature profile of the gas mixture from the LB simulation (symbols) with the analytical solution (lines), at different time steps. The simulation details are given in the text.

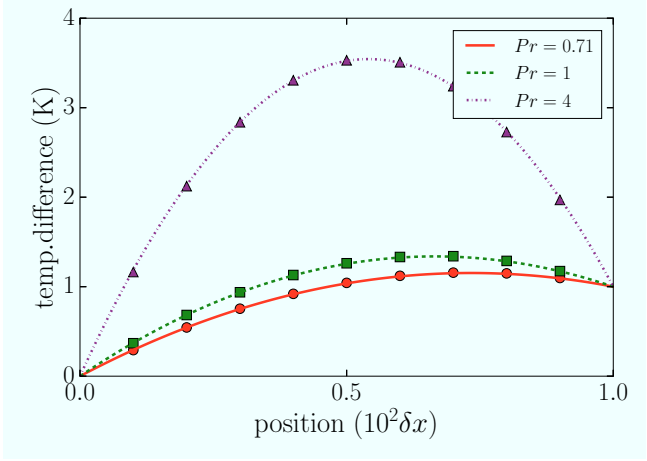


FIG. 6. Thermal Couette flow in a mixture of 0.01% H_2, 49.99% H_2O, 49.99% CO and 0.01% CO_2: comparision of the steady-state temperature profile resulting from the LB simulation (symbols) and the analytical solution (lines). Viscosity and thermal conductivity of the individual components is calculated consistently from the Lennard-Jones parameters. The Prandtl number is adjusted with the help of Eq. (46).

case, the gas mixture is placed between two parallel walls, but now with the warmer wall moving tangential to the fluid domain with a wall velocity $U_w = 0.1$ in (L.B units) and with a small temperature difference of $\Delta T = 1$ K between the two plates. Again, diffusive boundary conditions are applied to both plates, and periodic boundary conditions are applied in the flow direction.

The Navier-Stokes equations predict the steady-state temperature profile to be a function of the Prandtl number as

$$T(x) = T_C + \frac{PrU_w^2}{c_p \Delta T} \frac{y}{L}\left(1 - \frac{y}{L}\right), \tag{65}$$

with $c_p = 2$ (in LB units) being the isobaric heat capacity of the ideal gas in two dimensions.

Fig. 6 shows the simulation results for three different Prandtl numbers ($Pr = 0.71, 1, 4$). $Pr = 0.71$ is a typical value for a gas at ambient conditions, while $Pr = 1$ when no Prandtl number correction is applied ($\Phi_{ji}^{Pr} = 0$), and $Pr = 4$ when no energy correction at all is applied ($\Phi_{ji}^{Pr} = 0$ & $\Phi_{ji} = 0$). The agreement with the analytical solution (Eq.(65)) is excellent over the whole simulation domain, which shows the quality of the overall model and in particular the correctness of the correction terms derived in Sec. III.

V. THERMAL DIFFUSION ACROSS A SOLID-FLUID INTERFACE

In order to accurately capture effects like heat accumulation two ingredients are needed: (i) the thermal conduction though the solid and (ii) coupling of the temperature fields across the solid-fluid interface. The thermal conduction within the solid is described by the heat equation

$$\partial_t T = -\alpha_s \nabla^2 T, \tag{66}$$

with α_s being the thermal diffusivity within the solid. In this paper the heat equation is solved with a second-order forward Euler finite difference (FD) scheme. To avoid additional computational overhead for interpolation the identical real-space lattice and time integration step δt as for the LB simulation are used. The time propagation along each lattice direction is evaluated in each LB iteration as

$$T_x^s(t + \delta t) = T_x^s(t) + \alpha_s T^{s''}_x(t), \tag{67}$$

where the second derivative

$$T^{s''}_x(t) = T^s_{x-1}(t) - 2T^s_x(t) + T^s_{x+1}(t), \tag{68}$$

is calculated from central finite differences of the solid temperature T^s for each solid node x.

For $\alpha_s > 0.5$ the stability of the forward Euler scheme is challenged. For such values a fully explicit scheme, e.g. Crank-Nicholson, is recommended. Extending the current implementation into this direction is straightforward. In this study, however, we focus on the applications of porous silicate, in which α_s is of the same order as the thermal diffusivity in the gas domain. The stability of the overall scheme is therefore governed by the stability of the LBM part, i.e. the range of values for τ_1. Or in other words: In this combined FD-LBM scheme the LBM time step is very small anyway, such that the FD part is stable.

Using the same lattice for the FD as well as for the LBM calculation allows for a simple definition of

Dirichlet-like boundary conditions in each iteration: For the calculation of the second derivative close to the interface, we simply include the temperature from the neighboring fluid nodes entering Eq. (68). This already leads to an intrinsic coupling between the solid and the fluid domain, as any temperature difference between solid and fluid affects the solid temperature via Eq. (68).

Coupling of the solid temperature to the temperature field in the fluid domain is realized through the diffusive boundary conditions (Eq. (61)), where the wall temperature T_w is a function of the temperature of the first solid node T^s, the first fluid node T^f, and of the respective heat diffusivities. Here, we suggest a general combination

$$T_w = \frac{T^s + T^f}{2} + \gamma(\alpha_s, \alpha_t)\big(T^s - T^f\big), \tag{69}$$

where the first term is the average between the solid and fluid temperature at the interface. The second term is a temperature gradient term which is scaled with a parameter γ, reflecting the time scale for thermal diffusion. We find a value of $\gamma = 3\frac{\alpha_s+\alpha_f}{2}$ to minimize discontinuities of the temperature profile and its first and second derivatives across the interface.

The two coupling mechanisms described, however, do not conserve the thermal energy. This is even more aggravated by the fact that the level of dereliction of energy conservation strongly depends on the solid ratio in the system: since in the LBM the fluid is almost incompressible, a temperature gradient always induces a pressure wave. This pressure wave transports thermal energy, however, at the speed of sound, which is a mechanism not captured by Eq. (66). Besides the correct thermal diffusion, any temperature gradient at the interface heats the fluid through this mechanism as well. The fluid domain inevitably heats up faster than the solid domain leading to the observed dependence on the solid ratio.

A simple and parameter free correction can be realized by subtracting the heat flux $\vec{q}$ through the interface with the interface normal $\vec{n}$ integrated over time δt:

$$T_x^s(t+\delta t) = T_x^s(t+\delta t) - \frac{1}{c_p \rho}|\vec{q}(t)\cdot\vec{n}|\delta t, \tag{70}$$

where the heat flux $\vec{q}$ is calculated from the gradient of the temperature

$$q_\alpha = \kappa \partial_\alpha T. \tag{71}$$

The quality of the overall thermal coupling through the interface (incl. Eq. (67), Eq. (61) with Eq. (69) & and Eq. (70)) is scrutinized in a quasi 1-dimensional test system (with 200×3 lattice sites), which consists of a solid and a fluid domain. Periodic boundary conditions are applied in all four directions, hence comprising two solid-fluid interfaces. Reactive boundary conditions at the interface catalyze the exothermic water-gas-shift reaction ($CO + H_2O \longrightarrow H_2 + CO_2$). The corresponding heat change is the reaction enthalpy ΔH_r times the molar change of the reactant, e.g. CO. The response of the system is measured by calculating the change of temperature in the fluid and the solid domain, which allows to define the error in enthalpy conservation as

$$\varepsilon = \frac{c_p(T - T_0) - \Delta H_r \cdot \Delta C_{CO}}{\Delta H_r \cdot \Delta C_{CO}} \quad . \tag{72}$$

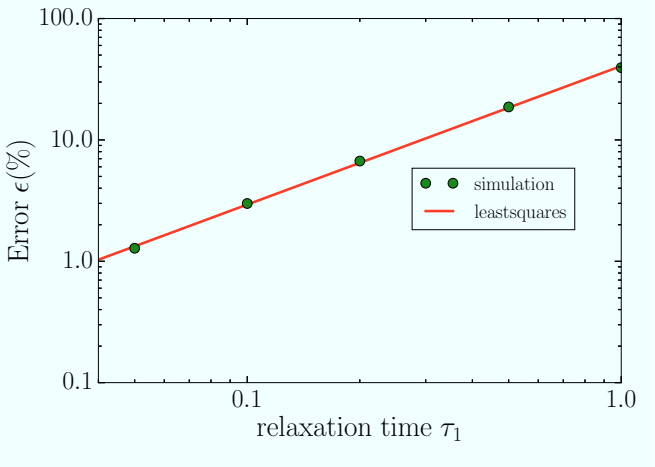


FIG. 7. Error analysis of the thermal coupling between solid and fluid domain: the black-dashed line is a least-squares fit to the simulation results (purple), showing a power-law dependence of the error ϵ on the relaxation time τ_1 (which is related to the thermal conductivity) of $\epsilon = 40.65 \times \tau^{1.14}$. Simulation details are given in the text.

To asses the dependence from the thermal diffusivities, the error ε is measured for a wide range of relaxation times τ_1. The error is plotted on a double-logarithmic scale in Fig. 7, revealing a power law dependence. The slope is determined as 1.14 and shows that the proposed coupling scheme is essentially first-order accurate. The scheme can in principle be improved beyond first-order accuracy by calculating the first and second derivatives from higher-order finite differences. We, however, find that higher-order terms can lead to temperature oscillations in the fluid domain, which destructively resonate with the correction term Φ around corner sites. This limits its numerical stability to high thermal diffusivities, where such oscillations are in the overdamped regime.

We test the generality and transferabilty of the coupling scheme employing a variety of simulation domain configurations over a wide range of sensible values for applications in chemical reactors. We find that the dependence on the system size (if larger than $N = 20$) and the solid fraction is negligible. The observed error is also independent of the initial temperature T_0 and independent of the reaction rate and the reaction enthalpy. We also measure that the enthalpy uptake of the solid and the fluid fraction is in very good agreement with the respective heat capacities.

VI. SHOWCASE

As a showcase for the overall model we present simulation results of a model fixed-bed reactor consisting of six cubes of different sizes with quasi-random distribution. The simulation domain was discretized on a lattice with $N_x \times N_y = 600 \times 200$ lattice nodes, assuming a resolution of 5 μm per lattice unit. The edge length of the cubes is as low as 200 μm showing the applicabilty of the scheme for micro-porous material. The surface of the cubes catalyses the water-gas-shift reaction, involving a gas species with very different viscosities, diffusivities and masses, rendering this a highly diagnostic set-up to scrutinize the scheme. Boundary conditions at the inlet (left side) are designed to ensure a continuous flow of constant temperature (403 K), constant pressure (1 bar), constant flow velocity ($u_x = 0.001 = 2.2$ m/s) in positive x-direction and a constant molar fraction of 49.999% of the CO and H_2O and 0.001 % of H_2 and CO_2. Quasi-zero gradients at the outlets are realized by copying the populations from the last fluid node and all correction terms are set to zero in a vicinity of three lattice nodes around the inlet and outlet. Periodic boundary conditions are applied in y-direction. The dynamic viscosities (thermal conductivities) and the binary diffusion coefficients of each species are calculated from the Lennard-Jones parameters of the gas, at given local conditions. For the material properties of the solid nodes we use typical values of silica, with a density $\rho^s = 2000$ kg/m^3 and a specific heat of $c_p^s = 0.7$ kJ/kg/K. The thermal conductivity within the solid cubes is set to $\alpha_s = 0.046 = 2.2 \times 10^{-5} m/s^2$.

The reaction term S_j is calculated from the rate constant k given by the Arrhenius equation ($k = A \exp[-E_a/k_b T_w]$) at the given local wall temperature, the reactant concentrations at the wall and the molar masses

$$S_j = \pm M_j k \cdot C_{CO} C_{H_2O} \cdot \sqrt{\frac{M_0}{M_j}}. \qquad (73)$$

The minus sign is used for reactants and the plus sign for product species. Note that the last factor stems from the fact that S_j corresponds to a mass flux and not a mass density, and therefore requires the same scaling as the microscopic velocities at c_j. We use an activation energy E_a of 84 kJ/mol taken from literature [40]. For the purpose of a showcase, we use a large value for the prefactor A of 10^6 m/s and scale the reaction enthalpy $\Delta H_r = -41$ kJ/mol with a factor of 10^2.

The given inlet and outlet boundary conditions lead to a flow profile as shown in the Fig. 8 (a). The solid cubes constrain the gas flow through a network of small channels (pores), which locally increases the flow velocity. The effect of the reactive boundary conditions can be seen in Fig. 8 (b) and (c). The molar fractions of the two product species H_2 and CO_2 increase at the surface of the solid cubes, and are then transported away by the gas stream. The product concentration is highest

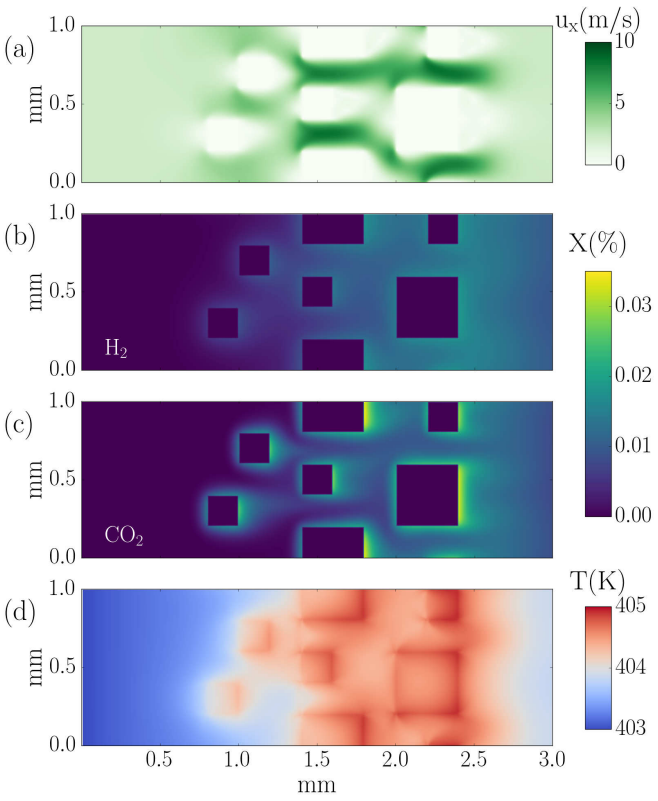


FIG. 8. Reactive flow through a model porous network. The contour maps show the velocity field (a), molar fractions of the products H_2 (b) and CO_2 (c) and the temperature profile (d) after 150'000 time steps. The surface of the cubes catalyzes the water-gas-shift reaction. The inlet is on the left side and outlet on the right, periodic boundary conditions are applied in y-direction.

on the backside of the cubes. There, the flow velocity is low, which leads to an accumulation of the product species. This effect is much more pronounced for the heavier CO_2. The amount of both product species, i.e. the concentrations integrated over the entire simulation domain, are equal to within 1%, which shows the quality of mass conservation even for large mass ratios. The local concentrations, however, deviate significantly, which is due to fact that the diffusion coefficient of H_2 is larger by a factor of five as compared to CO_2. This exemplifies the complexity of the reactive gas flow through microporous material.

A similar complexity is also visible in the temperature field as shown in the Fig. 8 (d). Along with the change of chemical composition the reaction at the surface releases reaction enthalpy, which heats up the surface of the solid cubes. On the one hand the heat is conducted into the solid domain, and raises the temperature. On the other hand, the heat diffuses into the fluid domain and is transported away efficiently by the flow field. While there is a general increase in temperature in flow direction (from left to right), the detailed features on the surface of the

cubes are rich. The highest temperature regions agree to those with highest product concentration, namely the backside of the cubes. Here, the flow velocities are smallest which in turn leads to diffusion limited heat transport. The fact that the temperature significantly decreases towards the outlet shows that the snapshots in Fig. 8 do not correspond to steady state conditions.

We want to stress that the temperature increase is to the vast extend due to the reaction enthalpy. However, local temperature variations of up to 0.4 K also appear due the dynamic pressure around the obstacles. While this effect is to most extend physically justified it also leads to minor artifacts around the corner sides of the cubes, which stems from the large flow velocities and therefore large gradients around the corner. These artifacts can be suppressed by decreasing the flow velocity or through grid refinement.

VII. CONCLUSIONS

We presented a hybrid finite-difference LBM scheme for the study of enthalphy consistent catalytic flows through porous media. The gas phase domain is solved with a multicomponent thermal LBM similar to the model by Kang et al. [16]. However, the applied correction terms deviate from the original work. We showed that our correction terms ensure the correct macroscopic mass and heat transport behaviour of the flow. Reactive boundary conditions are used to simulate a chemical reaction at the surface of an obstacle in a very flexible way. The reaction enthalpy consistently heats up the fluid as well as the solid domain, where the heat equation is solved through finite-differences. We showed that the proposed coupling mechanism for the enthalpy is first-order accurate. In a final showcase we exemplified the application in form of a catalytic flow simulation through a model porous material, revealing rich information of the local temperature and molar fraction distributions.

We demonstrated application for a model porous material consisting of plane and convex corner surface nodes. To model arbitrary surfaces concave corner sites are necessary. As discussed above, the interpolation in the direct vicinity of concave corner sites are ill-defined, since neighboring off-lattice populations are not present. To this end a consistent and convincing remedy is still missing, and will be the subject of a future project. Concave corner sites can however be used without issues when the interpolation is not performed for the critical populations.

In applications resembling real systems with defined system size, temperature, pressure and flow velocity a reasonable value for grid spacing δx in SI units has to be chosen. Together with the velocity scale, which is defined by the temperature and molar mass of the lightest element, the grid spacing also defines the time step δt in SI units. Small length scales thereby imply small time steps. For the showcase example in Sec. VI the grid resolution of $\delta \mathrm{x} = 5\mu$ yields a time step of $\delta t = 2ns$. This of course limits the applicabilty when slow processes are to be observed on small length scales. On the other hand, fast processes require a reasonable time resolution which requires a high grid resolution. The grid resolution is ultimately limited by the Knudsen number of the system. In the case of large Knudsen numbers ($Kn > 1$) intramolecular collision is not the dominant mechanism for relaxation towards the thermodynamic equilibrium. For such cases alternative strategies have to be implemented. As discussed in Sec. VI the value of applicable flow velocities is limited, at least for complex geometries where corner sites lead to temperature and pressure artifacts. While such artifacts can be suppressed by increasing the grid resolution (within limits discussed above) this comes at a price of decreased time steps.

ACKNOWLEDGMENTS

The authors thank Dr. Nikolaos I. Prasianakis for instructive discussions. The authors further thank Dr. David Smith, Dr. Marco Haumann, Dr. Peter Wasserscheid and Dr. Nadiia Kulyk for fruitful discussions. The authors acknowledge financial support by the Deutsche Forschungsgemeinschaft (DFG) within the Cluster of Excellence "Engineering of Advanced Materials"(project EXC 315) (Bridge Funding).

Appendix A: Dynamic viscosities and binary diffusion coefficients

The dynamic viscosity of each species j with the molar mass M_j is calculated from the Lennard-Jones parameters of the idealized gas σ_j according to Eqs. (7–10) in Ref. 32:

$$\mu_j = 2.67 \times 10^{-6} \frac{\sqrt{M_j T}}{\sigma_j^2 \Omega_\mu}, \tag{A1}$$

$$D_{jk} = 1.86 \times 10^{-3}\ T^3\ \frac{\sqrt{\frac{1}{M_j} + \frac{1}{M_k}}}{P \sigma_{jk}^2 \Omega_D}. \tag{A2}$$

The collision integrals Ω_D and Ω_μ are a function of the the Lennard-Jones parameters and the temperature. We evaluate those values from a spline function based on the tabulated values from Appendix K in Ref. 32.

Appendix B: Dimensions

The actual simulations runs in simulation units, which have to be properly related to SI units via the laws of the ideal gas together with the lattice spacing: The characteristic velocity of an ideal gas of molar mass M_j and

temperature T_0 is given in SI units by

$$U = \sqrt{\frac{3RT_0}{M_j}}, \tag{B1}$$

where R is the gas constant. In internal LB units the characteristic velocity U is equal to the lattice velocity c_{ji}. The lightest element is streamed on-lattice ($c_0 = 1$) and therefore sets the velocity scale

$$U' = \frac{U(M_0)}{c_0} = \sqrt{\frac{3RT_0}{M_0}}. \tag{B2}$$

The temperature scale in lattice units is defined with respect to a reference temperature, which is set to $1/3$ in lattice units ($T' = T_0/(1/3)$). The length scale is readily defined by the characteristic length in physical units L and the discretized characteristic length in lattice units L_{LB}

$$L' = \frac{L}{L_{LB}}. \tag{B3}$$

The time scale is then calculated from the velocity and length scales as

$$t' = \frac{L'}{U'}. \tag{B4}$$

Conversion factors for the pressure, viscosity and binary diffusion coefficients can be derived in a similar way,

$$\mu' = L'U', \quad D' = L'U', \quad P' = U'U', \tag{B5}$$

while the density is set to have the same values as in SI units ($\rho' = 1$).

[1] A. Corma, Chem. Rev. **97**, 2373 (1997).
[2] J. Lee, O. K. Farha, J. Roberts, K. A. Scheidt, S. T. Nguyen, and J. T. Hupp, Chem. Soc. Rev. **38**, 1450 (2009).
[3] C. P. Mehnert, Chem. Eur. J. **11**, 50 (2005).
[4] R. Benzi, S. Succi, and M. Vergassola, Phys. Rep. **222**, 145 (1992).
[5] T. Krüger, H. Kusumaatmaja, A. Kuzmin, O. Shardt, G. Silva, and E. M. Viggen, *The Lattice Boltzmann Method* (Springer, 2017).
[6] H. Liu, Q. Kang, C. R. Leonardi, S. Schmieschek, A. Narváez, B. D. Jones, J. R. Williams, A. J. Valocchi, and J. Harting, Comput. Geosci. **20**, 777 (2016).
[7] X. He, S. Chen, and G. D. Doolen, J. Comput. Phys. **146**, 282 (1998).
[8] A. Scagliarini, L. Biferale, M. Sbragaglia, K. Sugiyama, and F. Toschi, Physics of Fluids **22**, 055101 (2010).
[9] Y. Peng, C. Shu, and Y. T. Chew, Phys. Rev. E **68**, 026701 (2003).
[10] Z. Guo, C. Zheng, B. Shi, and T. S. Zhao, Phys. Rev. E **75**, 036704 (2007).
[11] N. I. Prasianakis and I. V. Karlin, Phys. Rev. E **76**, 016702 (2007).
[12] X. Shan and G. Doolen, J. Stat. Phys. **81**, 379 (1995).
[13] X. Shan and G. Doolen, Phys. Rev. E **54**, 3614 (1996).
[14] S. Arcidiacono, I. V. Karlin, J. Mantzaras, and C. E. Frouzakis, Phys. Rev. E **76**, 046703 (2007).
[15] J. Kang, N. I. Prasianakis, and J. Mantzaras, Phys. Rev. E **87**, 053304 (2013).
[16] J. Kang, N. I. Prasianakis, and J. Mantzaras, Phys. Rev. E **89**, 063310 (2014).
[17] S. Arcidiacono, J. Mantzaras, and I. V. Karlin, Phys. Rev. E **78**, 046711 (2008).
[18] Supplementary material available on the journal homepage.
[19] Y. Qian, D. d'Humières, and P. Lallemand, EPL **17**, 479 (1992).
[20] A. N. Gorban and I. V. Karlin, Physica A **206**, 401 (1994).
[21] C. D. Levermore, J. Stat. Phys. **83**, 1021 (1996).
[22] P. L. Bhatnagar, E. P. Gross, and M. Krook, Phys. Rev. **94**, 511 (1954).
[23] S. Ansumali, S. Arcidiacono, S. Chikatamarla, N. Prasianakis, A. Gorban, and I. Karlin, Eur. Phys. J. B **56**, 135 (2007).
[24] Y.-H. Qian and Y. Zhou, EPL **42**, 359 (1998).
[25] S. S. Chikatamarla and I. V. Karlin, Phys. Rev. Lett. **97**, 190601 (2006).
[26] R. Rubinstein and L.-S. Luo, Phys. Rev. E **77**, 036709 (2008).
[27] S. Chapman and T. G. Cowling, *The mathematical theory of non-uniform gases: an account of the kinetic theory of viscosity, thermal conduction and diffusion in gases* (Cambridge university press, 1970).
[28] R. B. Bird, W. E. Stewart, and E. N. Lightfoot, *Transport phenomena* (John Wiley & Sons, 2007).
[29] E. S. Oran and J. P. Boris, Prog. Energy Combust. Sci. **7**, 1 (1981).
[30] T. Coffee and J. Heimerl, Combust. Flame **43**, 273 (1981).
[31] C. Wilke, J. Chem. Phys. **18**, 517 (1950).
[32] J. R. Welty, C. E. Wicks, G. Rorrer, and R. E. Wilson, *Fundamentals of momentum, heat, and mass transfer* (John Wiley & Sons, 2009).
[33] Here we use the identity $\frac{1}{C} = \frac{M}{\rho}$ for the conductive term in Eq. (41).
[34] Q. Kang, P. C. Lichtner, and D. Zhang, Water Resour. Res. **43** (2007).
[35] L. Chen, Q. Kang, B. A. Robinson, Y.-L. He, and W.-Q. Tao, Phys. Rev. E **87**, 043306 (2013).
[36] T. Zhang, B. Shi, Z. Guo, Z. Chai, and J. Lu, Phys. Rev. E **85**, 016701 (2012).
[37] V. Sofonea and R. F. Sekerka, J. Comput. Phys. **207**, 639 (2005).
[38] S. Ansumali, I. Karlin, C. E. Frouzakis, and K. Boulouchos, Physica A **359**, 289 (2006).
[39] M. Hecht and J. Harting, J. Stat. Mech. Theory Exp. **2010**, P01018 (2010).
[40] S. Werner, N. Szesni, R. W. Fischer, M. Haumann, and P. Wasserscheid, Phys. Chem. Chem. Phys. **11**, 10817

(2009).